PCCP

Physical Chemistry Chemical Physics

rsc.li/pccp

ROYAL SOCIETY
OF CHEMISTRY

PAPER
Tommy Nylander, Costanza Montis *et al*.
Interaction of nanoparticles with lipid films: the role of
symmetry and shape anisotropy

PCCP

Check for updates

Interaction of nanoparticles with lipid films: the role of symmetry and shape anisotropy†

Lucrezia Caselli,[a] Andrea Ridolfi, [ID] [ab] Gaetano Mangiapia, [ID] [c]
Pierfrancesco Maltoni, [ID] ‡[a] Jean-François Moulin, [ID] [c] Debora Berti, [ID] [a]
Nina-Juliane Steinke,§[d] Emil Gustafsson,[e] Tommy Nylander [ID] *[fg] and
Costanza Montis [ID] *[a]

The bioactivity, biological fate and cytotoxicity of nanomaterials when they come into contact with living organisms are determined by their interaction with biomacromolecules and biological barriers. In this context, the role of symmetry/shape anisotropy of both the nanomaterials and biological interfaces in their mutual interaction, is a relatively unaddressed issue. Here, we study the interaction of gold nanoparticles (NPs) of different shapes (nanospheres and nanorods) with biomimetic membranes of different morphology, *i.e.* flat membranes (2D symmetry, representative of the most common plasma membrane geometry), and cubic membranes (3D symmetry, representative of non-lamellar membranes, found in Nature under certain biological conditions). For this purpose we used an ensemble of complementary structural techniques, including Neutron Reflectometry, Grazing Incidence Small-Angle Neutron Scattering, on a nanometer lengthscale and Confocal Laser Scanning Microscopy on a micrometer length scale. We found that the structural stability of the membrane towards NPs is dependent on the topological characteristic of the lipid assembly and of the NPs, where a higher symmetry gave higher stability. In addition, Confocal Laser Scanning Microscopy analyses highlighted that NPs interact with cubic and lamellar phases according to two distinct mechanisms, related to the different structures of the lipid assemblies. This study for the first time systematically addresses the role of NPs shape in the interaction with lipid assemblies with different symmetry. The results will contribute to improve the fundamental knowledge on lipid interfaces and will provide new insights on the biological function of phase transitions as a response strategy to the exposure of NPs.

Introduction

Living organisms are increasingly exposed to nanomaterials, either intentionally administered or unintentionally released in the environment. The interaction of nanosystems with

[a] *Department of Chemistry, University of Florence and CSGI, Florence, Italy.*
 E-mail: costanza.montis@unifi.it
[b] *ISMN-CNR and CSGI, Bologna, Italy*
[c] *German Engineering Materials Science Centre (GEMS) at Heinz Maier-Leibnitz Zentrum (MLZ), Helmholtz-Zentrum Hereon, Lichtenbergstr. 1, 85748 Garching bei München, Germany*
[d] *ISIS, Rutherford Appleton Laboratory Didcot, Oxfordshire, UK*
[e] *Department of Chemistry, Uppsala University, Uppsala, Sweden*
[f] *Department of Chemistry, Physical Chemistry, Lund University, Lund, Sweden.*
 E-mail: tommy.nylander@fkem1.lu.se
[g] *NanoLund, Lund University, Lund (Sweden, Lund Institute of Advanced Neutron and X-Ray Science - LINXS), Lund, Sweden*
† Electronic supplementary information (ESI) available: Supplementary Materials and Methods and data analysis. See DOI: 10.1039/d1cp03201a
‡ Current affiliation: Department of Materials Science and Engineering, Uppsala University, Uppsala, Sweden.
§ Current affiliation: Institut Laue-Langevin, Grenoble, France.

Costanza Montis

Costanza Montis is Assistant Professor of Physical Chemistry at the Department of Chemistry, University of Florence, and member of the Italian Consortium for Colloid and Surface Science (CSGI). She received her PhD in Chemical Sciences from the University of Florence in 2013. Her main research activity focuses on the understanding of complex phenomena occurring at interfaces, from a physicochemical perspective. Her scientific interests are in physical chemistry of soft matter and include the biophysical understanding of nano-bio interfaces; the design of lipid-nanoparticles hybrid materials for biomedical applications; the engineering/characterisation of biogenic extracellular vesicles; the study of nanostructured materials for applications in restoration of works of art.

biological matter proceeds through an intricate balance of forces,[1–3] occurring at the nano-bio interface, where nano-materials, *e.g.* nanoparticles, meet biological fluids and barriers (such as biological membranes). Disentangling these contributions is key to understand the fate of the nanoparticles in living systems, in particular their toxic effects and, concerning nanomaterials designed for nanomedicine, their efficacy in reaching their biological target.[4–10] In this context, where multiple factors and forces are simultaneously at play, the concept of symmetry, which can be related both to the shape of NPs and to the nanoscale structure of the target biological membrane, is particularly interesting.

The role of NPs shape asymmetry is currently the focus of extensive research. Both experimental and computational studies highlight that the anisotropy of NPs is a determining factor in their internalization pathways in cells.[4,11–15] In particular, NPs shape modifies the area available for NPs adsorption on lipid surfaces,[16] therefore modulating the strength of NP-membrane adhesion forces. Additionally, topological effects are significant in the surface functionalization of NPs (*e.g.*, ligand surface density), affecting their chemical identity.[17] Finally, a high surface curvature, either uniformly distributed on the surface of NPs (*e.g.*, small NPs with sizes of a few nm) or localized at the sharp edges of asymmetric NPs (*e.g.*, nanorods), is associated to higher energetic costs in terms of wrapping and internalization by membranes.[3,12,14,15] Anisotropic NPs, unlike spheres, can reorient in proximity to the lipid interface to minimize this energy penalty and maximize the adhesion strength to the membrane.[18]

On the other side, biological membranes are commonly characterized by a planar geometry with a bidimensional structure, *i.e.*, an infinite plan constituted by a lipid bilayer. However, such arrangement can undergo striking temporary or permanent topological modifications in selected conditions, for instance in cell trafficking phenomena or in pathological conditions, often related to a significant symmetry alteration. In particular, curved membrane configurations characterized by a 3D symmetry, as cubic bicontinuous arrangements, are known to occur in cells under pathological conditions (*e.g.*, drug detoxification, starving, infection, oxidative stress, and cancer disease) or during certain phases of cell life (*e.g.* membrane fusion).[19–21] Up to now, the investigations related to these so-called "cubic membranes" have been limited to a descriptive level, while their biological function remains practically unexplored.[20,21] This is mainly due to the transient nature of non-lamellar biological membranes, which makes their investigation in natural systems very challenging.[21] In this framework, lipid models of synthetic nature, mimicking cubic membranes structure, can be used to simplify the investigation. Our recent findings[22–24] show that it is possible to obtain solid-supported lipid model surface layers of cubic symmetry, with controlled physicochemical and structural features, enabling the study of NPs-cubic membranes interaction in highly simplified and controlled conditions.

Here we investigate how gold nanoparticles (AuNPs) of different symmetry (namely gold nanospheres (AuNSs) and

gold nanorods (AuNRs)) but similar size and surface coating, interact with target lipid films of different internal structure (namely a lamellar phase, of 2D symmetry, and a cubic phase, of 3D symmetry). By combining neutron scattering techniques (Neutron Reflectivity and Grazing-Incidence Small-Angle Neutron Scattering (GISANS)) with Confocal Laser Scanning Microscopy (CSLM), we unravel NPs-lipid films interaction as a function of time, from few minutes to many hours, and at different lengthscales (from nanometers to micrometers).

Our results show that the shape and symmetry of both the NPs and the lipid mesophase are key factors in driving the mechanism and strength of NP–lipid film interaction. Overall, these findings improve our understanding of the nano-bio interface. In addition, this contribution provides potential insights into the role of cubic membranes in biological systems.

Results and discussion

Characterization of gold nanoparticles and lipid films of different symmetry

Cationic gold nanospheres (AuNSs) and nanorods (AuNRs) in water were prepared according to well-known synthetic routes.[25–28] The concentration of particles was determined by ICP-AES, as described in the ESI.† Fig. 1, Panel (a) shows the Small Angle X-ray Scattering (SAXS) profiles and Transmission Electron Microscopy (TEM) images of both AuNSs and AuNRs. SAXS of AuNSs were analysed with a spherical form factor with Schulz polydispersity. AuNSs were found to be polydisperse spheres (PD 0.4) with a metal core of 3.4 nm, in perfect agreement with TEM (d = 3.4 ± 0.6 nm). SAXS data of AuNRs were analysed applying a model with cylindrical form factor with a polydisperse cross section. The fitting parameters are consistent with 7.4 (length width^{-1}) aspect ratio nanorods (length 19.2 nm, diameter 2.6 nm (PD 0.2)), in line with TEM analysis (length 18 ± 5 nm, diameter 4 ± 1 nm). The cationic capping agents of AuNSs and AuNRs (mearcaptoundecyl-*N,N,N*-trimethyl ammonium bromide (TMA) and cetyltrimethyl ammonium bromide (CTAB), respectively) determine for both spheres and rods an overall positive zeta potential (+26 ± 1 mV for AuNSs, +45 ± 2 mV for AuNRs). In summary, both AuNSs and AuNRs are characterized by a net positive charge, which has been shown to result in a strong attractive interaction with zwitterionic phospholipid membranes, characterized by a slightly negative zeta potential.[1,29] In addition, spherical NPs are characterized by a diameter similar to the rods cross section diameter; therefore, the main difference between AuNSs and AuNRs is the strong asymmetry of AuNRs, with two curved surfaces (the poles), separated by a cylindrical body.

Lipid films on glass coverslips of different liquid crystalline structure were prepared by spin-coating *n*-hexane solutions of 1-monoolein (GMO) to produce a cubic phase film and of GMO/DOPC (1,2-dioleoyl-*sn*-glycero-3-phosphocholine) (50/50 mol%) to obtain a lamellar phase film. For CLSM experiments, a fluorescent hydrophobic dye (Nile Red, 0.1 mol% with respect
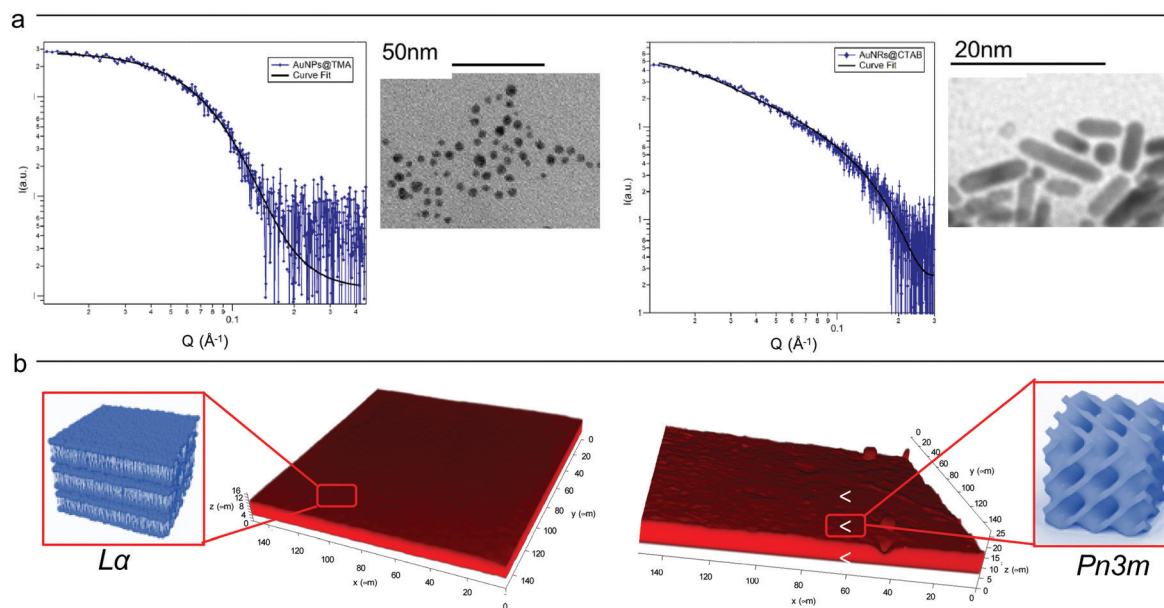
This journal is © the Owner Societies 2022

Phys. Chem. Chem. Phys., 2022, **24**, 2762–2776 | **2763**

Fig. 1 (Panel a) Physicochemical properties of NPs. Left: SAXS profile of AuNSs in water (at a concentration of 1.1×10^{15} particles mL^{-1}) and the corresponding fit with a Schulz polydisperse spheres model (see ESI,† for details). The inset shows a typical TEM image of AuNSs; Right: SAXS profile of AuNRs in water (at a concentration of 2.4×10^{14} particles mL^{-1}) and curve fitting according to a Cylinder poly radius model. The inset reports a TEM image of AuNRs; (Panel b) physicochemical properties of lipid films. Three-dimensional reconstruction of a confocal fluorescence z-stack of images of the lamellar (left side) and the cubic (right side) films (tilted surface area of 150×150 μm). The insets depict the lamellar Lα (left side) and cubic $Pn3m$ (right side) structures.

to the total lipid amount) was added. The lipid films were then dried in vacuum to completely remove the solvent and subsequently hydrated with an excess of water. Fig. 1, Panel (b), displays the 3D reconstructions of fully hydrated GMO and GMO/DOPC films. The morphology of the films at the micron-scale appears very similar, *i.e.*, a homogeneous thickness (of 10 ± 2 μm for both films), with low roughness. Due to the different compositions, it is expected that the lipid films are characterized by a different structural arrangement at a nanometric length scale: a $Pn3m$ cubic phase for GMO films and a Lα lamellar phase for GMO/DOPC films (see the schemes in Fig. 1b). This was confirmed by neutron reflectometry as described in the following section.

Nanoparticles–lipid films interaction at a nanometric lengthscale

GMO and GMO/DOPC films were formed on ultra-polished silicon blocks and fully hydrated with excess D_2O, they were then equilibrated for 12 h before characterisation with Neutron Reflectivity. Subsequently, AuNSs in D_2O were pumped in the measurement cell at a concentration of 3×10^{14} particles mL^{-1} (corresponding to 0.12 mg mL^{-1} gold concentration). It is worth noticing that, being lamellar and cubic films prepared with the same total amount of lipid, the same AuNSs concentration was employed to challenge lamellar and cubic films. Then, after 8 h incubation, the reflectivity curve for the lipid films in the presence of AuNSs was recorded.

The reflectivity profiles of GMO/DOPC (Fig. 2a) and GMO (Fig. 2b) films without NPs are consistent with the formation of highly ordered mesophases, with multiple Bragg reflections.

Also the detector images (inset in Fig. 2) show considerable off-specular scattering that reflects the structure of the lipid films. In particular, the reflectivity profile of the GMO-DOPC film features two prominent Bragg peaks located at 0.099 and 0.192 Å^{-1}, corresponding to the first two reflexes of the lamellar Lα phase. As sketched in Fig. 2a (left inset), the lamellar structure of the micrometric film consists of a stack of flat lipid bilayers separated by water layers. The unit cell spacing was calculated using the Q-position of the maximum intensity first-order reflexes[30] (see ESI,† for details), yielding a value of 64 ± 1 Å. This value is consistent with previous results obtained for a bulk GMO/DOPC Lα-phase.[31] Considering a thickness of about 34–37 Å for the GMO/DOPC bilayer (based on 37 Å and 34 Å for DOPC and GMO bilayers,[32,33] respectively), the water interlayers will have a thickness of 26–29 Å. The reflectivity profile of the GMO lipid film (Fig. 2b) presents at least two clearly distinguishable Bragg peaks, indicating also in this case a highly ordered internal structure. The position of these two peaks are at Q-values 0.091 and 0.111 Å^{-1}. These Q values can be associated to an inverse cubic phase with crystallographic space group $Pn3m$, corresponding to Miller indices (110) and (111). As depicted in the right inset, this structure has a bicontinuous nature, featuring a single lipid bilayer with negative curvature at the interface between lipid polar headgroups and water, which divides the inner space into two sets of interwoven aqueous channels. The lattice spacing d, calculated as described in the ESI,† is 95 ± 0.5 Å, corresponding to a water channel diameter of 44 Å,[34] similar to the diameter of the NPs.

When AuNSs are added to the GMO/DOPC film, the reflectivity still shows Bragg reflection peaks typical of the lamellar
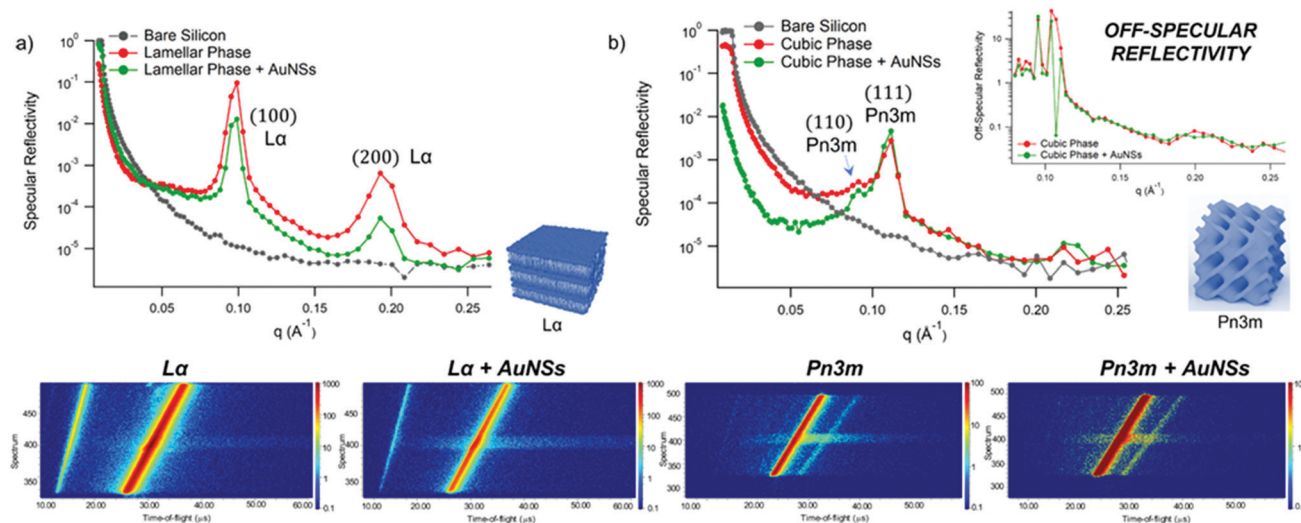
2764 | *Phys. Chem. Chem. Phys.*, 2022, **24**, 2762–2776

This journal is © the Owner Societies 2022

Fig. 2 (Panel a) Structural characterization of GMO/DOPC films interacting with AuNSs. Top: Specular reflectivity profiles of the GMO/DOPC film in the absence and in the presence of AuNSs, together with the reflectivity of the bare silicon. The inset sketches the inner Lα structure of the film; Bottom: Images of the reflectivity detectors acquired for the Lα phase in the absence and in the presence of AuNSs; (Panel b) structural characterization of GMO films interacting with AuNSs. Specular reflectivity of the GMO film in the absence and in the presence of AuNSs, together with the reflectivity of the bare silicon. The top inset represents the Off-specular reflectivity of GMO films in the absence and in the presence of AuNSs, while the bottom inset sketches the inner cubic $Pn3m$ structure of the lipid film; Bottom: Images of the reflectivity detectors acquired for the $Pn3m$ phase in the absence and in the presence of AuNSs. Measurements acquired at OFFSPEC,[55] ISIS Neutron and Muon Source (United Kingdom). The reflectivity profiles of lamellar and cubic films in the presence of AuNSs were acquired after 8 h of incubation, with 5 h acquisition time, leading to a lipid films/AuNSs total interaction time of 13 h.

arrangement. Although the positions are unchanged compared to before adding the particles, the presence of AuNSs produces a significant reduction in the peaks intensity. This suggests that a partial disruption of the bilayer arrangement occurs (a possible effect of lipid removal caused by the liquid flow through the sample cell had been previously ruled out with a control experiment, see ESI,† Fig. S4). However, the same AuNSs seem to have negligible impact on the nanostructure of the cubic lipid film: while a modification of the curve at low Q might suggest a variation of the overall film thickness and roughness, the presence of AuNSs does not significantly modify neither the position nor the intensity of the Bragg peaks, compared to the neat GMO film. This suggests that the nanostructure in the cubic film is stable and does not change even after 13 h of interaction (8 h of incubation + 5 h of measurement) with the AuNSs.

We further investigated the structure of AuNSs/cubic phase films by means of GISANS. The aim was to reveal possible effects of AuNSs on cubic phases, occurring over a longer time (8 h of incubation + 24 h of measurement, for a total AuNSs-membrane interaction time of 32 h). This technique allows also investigating the in-plane lipid arrangement and reveal how it changes upon AuNSs injection.[35] Lamellar films only have structural order with respect to the normal of the layers, while cubic phases are also characterized by high lateral ordering, whose possible modifications can be easily detected by GISANS. We performed GISANS on a neat GMO cubic film in D_2O, previously equilibrated for 12 h (Fig. 3a). Then, we added AuNSs at the same concentration as used for the Neutron Reflectivity measurements and left to incubate for 8 h.

The Q_z/Q_y GISANS pattern of GMO film in the absence of AuNSs shows isolated spots, which represent the (110) and (111) Bragg reflections of the $Pn3m$ structure. By performing horizontal line cuts (i.e. at constant Q_z) from the 2D GISANS plot, we determined the position of these highest intensity points (see Fig. S1 of ESI,† for details). The obtained Q values correspond to a $Pn3m$ cubic space group, with an obtained lattice parameter of 102 Å, in good agreement with the Neutron Reflectivity analysis. The presence of a spot-like pattern suggests a oriented cubic structure at the interface,[36] rather than a typical powder pattern that is mostly the case for the corresponding bulk GMO. The addition of AuNSs (Fig. 3b) smears out the spot-like pattern, which is now barely distinguishable from the Debye–Scherrer ring. This suggests a significant increase of the structural disorder within the mesophase, which can be either due to a partial disruption of the cubic symmetry or to a loss of spatial orientation, as well as loss of material from the surface. Interestingly, we also observed a significant shrinkage of the cubic phase lattice parameter in the presence of AuNSs (i.e., 2 nm) (see Fig. S2 of ESI†), implying a dehydration of the structure induced by AuNSs. In summary, GISANS data reveal a non-negligible impact of AuNSs on the cubic structure, when observed on longer time scales, thus complementing Neutron Reflectivity data. To conclude, for (relatively) short interaction times (Neutron Reflectivity data), the structural order of the lamellar mesophase decreases, while, in the same timeframe, the cubic phase mesostructure appears preserved. However, for longer incubation times (GISANS), AuNSs also affect the structural order of the cubic film. Therefore, the cubic mesophase appears significantly more stable than the lamellar one, when subjected to AuNSs exposure.
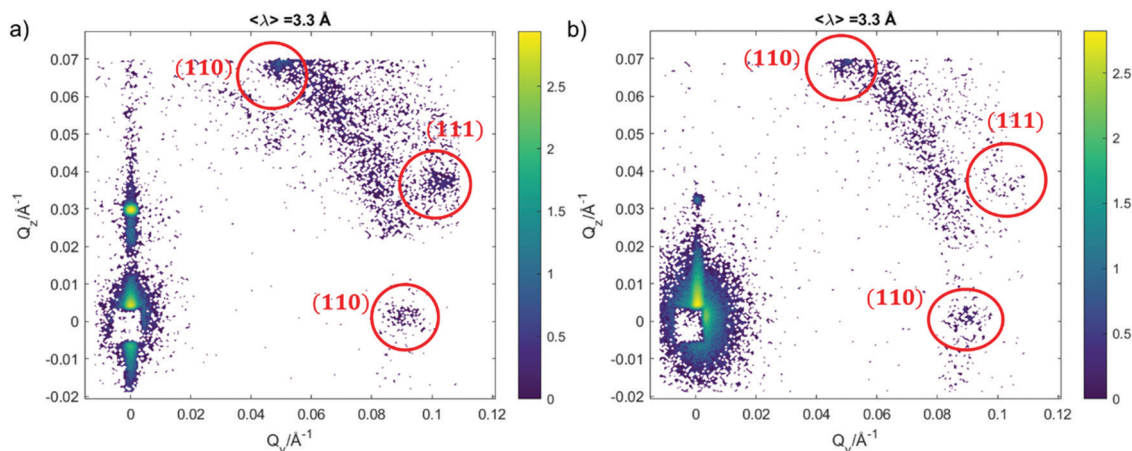
This journal is © the Owner Societies 2022

Phys. Chem. Chem. Phys., 2022, **24**, 2762–2776 | **2765**

Fig. 3 (a) GISANS pattern of GMO cubic *Pn3m* films, in the absence of NPs; (b) GISANS pattern of the GMO cubic *Pn3m* phase in the presence of AuNSs. Measurements acquired at REFSANS, Heinz Maier-Leibnitz Zentrum, Garching, Germany. In both the patterns, intensities are reported in a logarithmic scale. The reflectivity profiles of the cubic film in the presence of AuNSs was acquired after 8 h of incubation, with 24 h acquisition time, leading to a lipid film/AuNSs total interaction time of 32 h.

Fig. 4 shows Neutron Reflectivity data obtained for the same lipid films (lamellar in Fig. 4a and cubic in Fig. 4b) exposed to AuNRs at an Au concentration of 0.12 mg mL^{-1}, measured under the same experimental conditions as AuNSs. In contrast to AuNSs, AuNRs completely destroy both the lamellar and cubic arrangements, as evident from the absence of Bragg reflexes in the corresponding reflectivity profiles as well as in the reduced off-specular scattering in the inserted detector images. Indeed, for both the lamellar and the cubic film the Neutron Reflectivity profile of the remaining layer indicates a thickness consistent with a pure GMO or GMO/DOPC bilayer (curve fitting results are in the ESI,† Fig. S2). AuNRs and AuNSs

have similar size, *i.e.* similar cross section of the AuNRs and AuNSs diameter, and bear a net cationic surface charge. Therefore, the enhanced effect of AuNRs with lipid films suggests a strong role played by NPs shape asymmetry in the interaction with model lipid films.

Clearly, the drastic effect of AuNRs is not dependent on whether the film has a lamellar or a cubic phase structure, in the time frame of our experimental observations. To gain further insight on this fast disruption process, we performed Neutron Reflectivity kinetics studies, allowing for monitoring the structural alteration produced by AuNRs on shorter time scales.[37] We measured the reflectivity of lipid films in H$_2$O, just
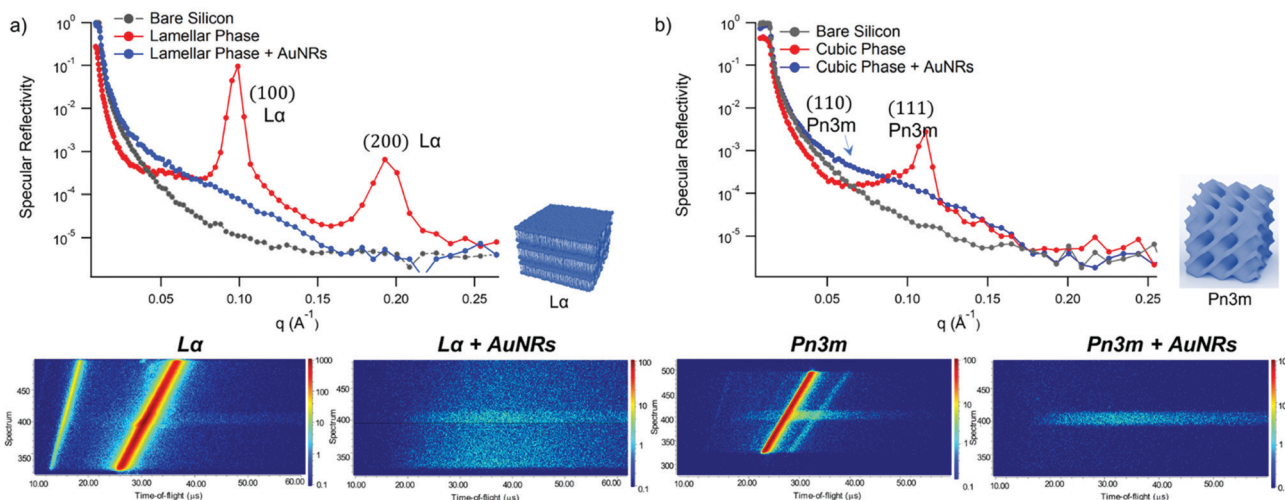

Fig. 4 (Panel a) Structural characterization of GMO/DOPC films interacting with AuNRs. Top: Specular reflectivity profiles of the GMO/DOPC film in the absence (red curve) and in the presence of AuNRs, together with the reflectivity of the bare silicon. The inset sketches the inner Lα structure of the film; Bottom: Detector images acquired for the Lα phase in the absence and in the presence of AuNRs; (Panel b) structural characterization of GMO films interacting with AuNRs. Specular reflectivity of the GMO film in the absence and in the presence of AuNRs, together with the reflectivity of the bare silicon. The inset sketches the inner cubic *Pn3m* structure of the lipid film; Bottom: Detector images acquired for the *Pn3m* phase in the absence and in the presence of AuNRs. Measurements acquired at OFFSPEC, ISIS Neutron and Muon Source (United Kingdom). The reflectivity profiles of lamellar and cubic films in the presence of AuNRs were after 8 h of incubation, with 5 h acquisition time, leading to a lipid films/AuNRs total interaction time of 13 h.

before and after the injection of AuNRs into the measuring cell, following the change in the reflectivity at time intervals of 2.5 min, covering a time period of 5 h. Representative data are shown in Fig. 5 as the (Q_z,Q_x) images from the reflectivity measurements for the lamellar (Panel a) and cubic film (Panel b), before and after AuNRs addition. The (Q_z,Q_x) maps of both lamellar and cubic films in the absence of NPs show pronounced off-specular patterns, featuring well defined "Bragg sheets" (see the red line in the left (Q_z,Q_x) plot of Panel b, as an example). The high intensity of the off-specular Bragg sheets allowed us to monitor the impact of AuNRs on the structure of lipid films over time. Panels a and b highlight a strong effect of AuNRs on both lamellar and cubic arrangements. The main effect is the smearing out of the characteristic Bragg sheets with time that ultimately leads to the complete loss of the off-specular signal. This indicates a total disruption of the films internal structure. Interestingly, lamellar films completely lose their structural organization significantly faster than cubic ones, with Braggs sheets completely vanishing within 12 min. In contrast, the cubic phase off-specular signal is still detectable after more than 2 h of incubation with AuNRs. Thus, cubic phases show larger structural stability when exposed to rods than lamellar ones. This is consistent with the previous reported effect of spherical particles.

In summary, Neutron Reflectivity and GISANS data allowed characterizing NPs-lipid films interactions at a nanoscale level,

revealing that: (i) AuNRs are more effective than AuNSs in inducing structural modifications in the lipid films (ii) cubic phases are more stable than lamellar phases. In this respect, the first point is consistent with other studies reported in literature. Indeed, several computational and experimental studies highlighted that AuNRs exhibit a stronger interaction with lipid membranes and that this a consequence of the anisotropic shape of NPs.[38,39] In addition, our results demonstrate that this behaviour of AuNRs does not depend the structure of the lipid assembly, *i.e.*, it applies both to planar membranes and to bilayers which are highly curved. On the other hand, the higher stability of cubic phases towards the interaction with NPs might be counterintuitive. In fact, cubic phase-nanoparticle dispersions (cubosomes) are known to be particularly prone to attach to target membranes, where lipid exchange can occur.[40] For the case with AuNP, the adhesion of NPs to an already curved membrane might be more favourable if the curvature of the particle matches that of the lipid aqueous interface. We further investigated this aspect on the micron-scale by studying the same systems with Confocal Laser Scanning Microscopy (CLSM). This allowed us to follow the morphological modification induced by NPs on lipid films.

Nanoparticles-lipid films interaction at a micrometer length scale

We performed the CLSM study over the same time frame of Neutron kinetics measurements. For this purpose, fluorescently
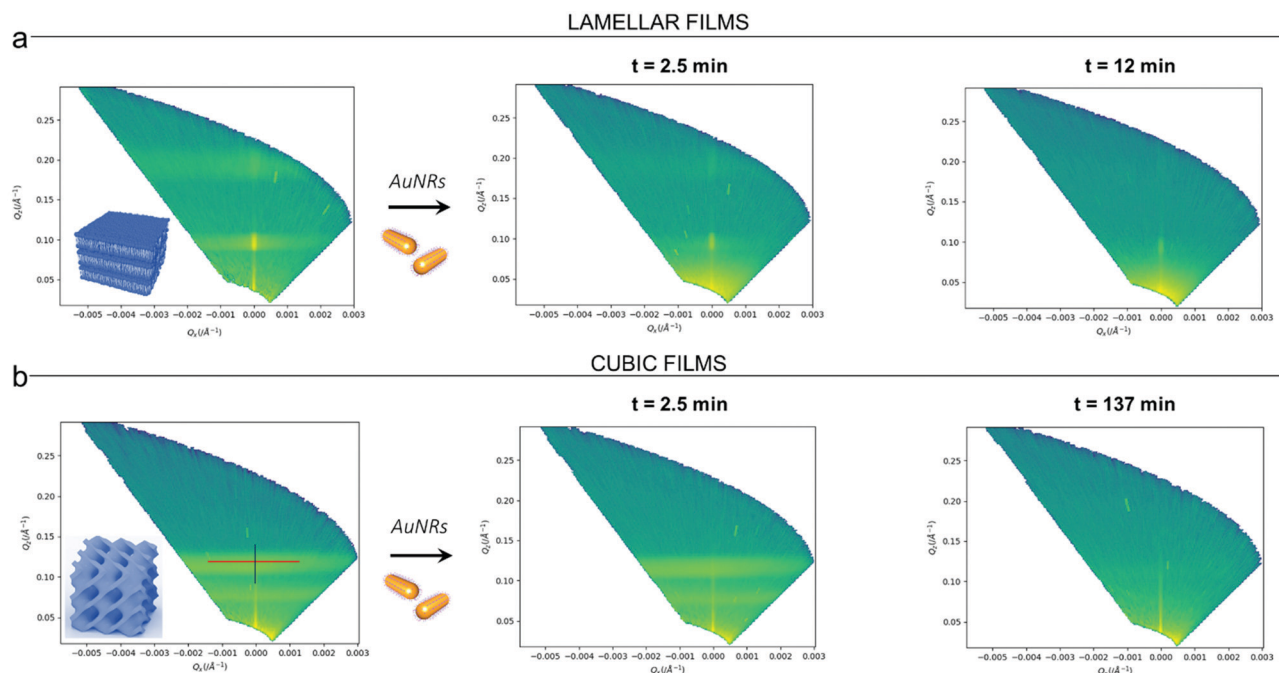

Fig. 5 (Panel a) Structural characterization of GMO/DOPC films interacting with AuNRs at short time-frames: (Q_z,Q_x) representations of the off-specular scattering of a lamellar film in the absence of AuNRs and at different times from the injection of AuNRs (acquisition in H_2O). (Panel b) Structural characterization of GMO films interacting with AuNRs at short time-frames: (Q_z,Q_x) representations enhancing the off-specular scattering of a cubic film in the absence of AuNRs and at different times from the injection of AuNRs (acquisition in H_2O). The integrated intensity along the specular reflectivity line (see blue line in the left (Q_z,Q_x) plot of Panel b) gives the specular reflectivity profile of lamellar and cubic films. Measurements of lamellar and cubic films in the presence of AuNRs were every 2.5 min with an acquisition of 5 min over 5 h, starting soon after the injection of AuNRs into the measurement chamber (incubation time ~ 0 s). Here, representative (Q_z,Q_x) representations acquired after 2.5 and 12 min (Panel a) or 2.5 and 137 min (Panel b) of lipid films/AuNRs incubation times are reported.

This journal is © the Owner Societies 2022

Phys. Chem. Chem. Phys., 2022, **24**, 2762–2776 | **2767**

labelled lamellar and cubic phases (Fig. 1, Panel b) were imaged right after (less than 1 s) and at different times after the injection of NPs. Fig. 6 gathers representative lateral-view CLSM images of a lamellar film exposed to AuNSs (Fig. 6a) and AuNRs (Fig. 6b). The action of spherical AuNSs (added at the same concentration employed in Neutron Reflectivity experiments) produces an initial swelling of the film (20 min), which increases the distance between the different lamellae composing the structure (Fig. 6a). This process leads to the progressive peeling-off of the lamellar film (60 min), with a gradual detachment of the outer surface layers. Once removed from the original matrix, these lipid layers start to bend and fold, ultimately rolling up in closed onion-like vesicular structures (180 min), which partially attach to the lipid film surface. After 180 min of incubation, only a thin layer of the original lamellar film is preserved onto the glass surface, partially covered by micron-sized multilamellar vesicles. The addition of asymmetrically shaped AuNRs (Fig. 6b) has a similar impact on the film morphology, which seems to progress in a similar way as with the AuNSs. However, the overall process is faster, consisting of an initial massive swelling of the lamellar membrane, which is observed after just 1 min from AuNRs addition. Moreover, the peeling-off of the film starts already after 5 min and, differently from the case of AuNSs, leads to the complete disruption of the lamellar film within 10 min, with only polydisperse vesicular structures remaining adsorbed onto the glass surface.

A completely different behaviour is observed when cubic phase lipid films are exposed to the same AuNPs. Spherical NPs

added at the same concentration (Fig. 7a) seem to "excavate" the cubic membrane, producing an initial thinning of the film over selected areas (see the highlighted area in Fig. 7a, 30 min). The progressive excavation leads to the formation of cavities, whose depth increases with time, eventually reaching the glass surface. After 180 min of incubation, the lipid film, although mostly intact, presents micron-sized holes, which are clearly highlighted from the 3D reconstruction of the film, reported in Fig. 7a. As previously observed for the case of lamellar membranes, the addition of AuNRs produces faster and more profound morphological modifications (Fig. 7b): AuNRs initially increase the films roughness (20 min), with the formation of "hills and hollows" across the micrometric membrane. Similarly to what was previously observed for spherical AuNSs, the lipid film is progressively excavated, showing micron-sized cavities, whose depth increases with time. However, in this case the erosion process is faster and progresses within a few minutes. Complete retraction of the cubic film occurs in localized areas on the glass substrate, giving rise to large spheres of lipid matrix (50 min). After 50 min, the lipid film is completely dewetted, leaving only isolated lipid spheres onto the glass substrate. Then, these lipid spheres are decomposed/removed due to the presence of the AuNRs (51 min).

The micrometric spheres disruption process, occurring within few seconds, can be analysed in detail, by following the temporal evolution of a horizontal section of the droplet. For this purpose, top-view images of a lipid droplet at different
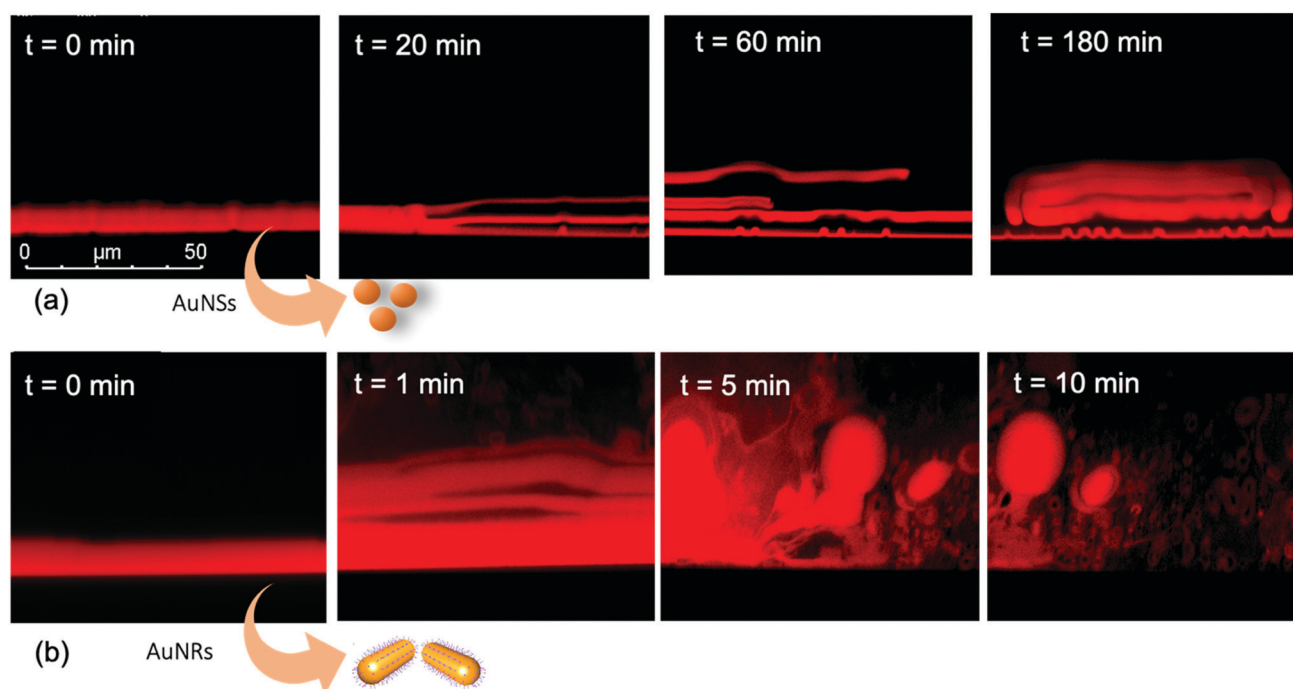

Fig. 6 (a) CLSM images (lateral view) of AuNSs interacting with a GMO/DOPC lamellar film. From left to right: lamellar film right after (t = 0 s), after 20 min, 60 min, and 180 min from the addition of AuNSs. (b) CLSM images (lateral view) of AuNRs interacting with a GMO/DOPC lamellar film. From left to right: lamellar film right after (t = 0 min), after 1 min, 5 min, and 10 min from the addition of AuNRs. Here, t = 0 corresponds to a lipid films/AuNPs incubation time $\sim$0 s, as the time needed for each image recording is less than 1 s.

Fig. 7 (a) CLSM images (lateral view) of AuNSs interacting with a GMO cubic film. From left to right: lamellar film right after (t = 0 min) and after 30 min and 180 min from the addition of AuNSs. A 3D reconstruction of the film after 180 min interaction is also shown, highlighting the presence of micron sized holes in the film. (b) CLSM images (lateral view) of AuNRs interacting with a GMO cubic film. From left to right: cubic film right after (t = 0 min) and after 20 min, 50 min, and 51 min from the addition of AuNRs. Here, t = 0 corresponds to a lipid films/AuNPs incubation time ∼0 s, as the time needed for each image recording is less than 1 s.
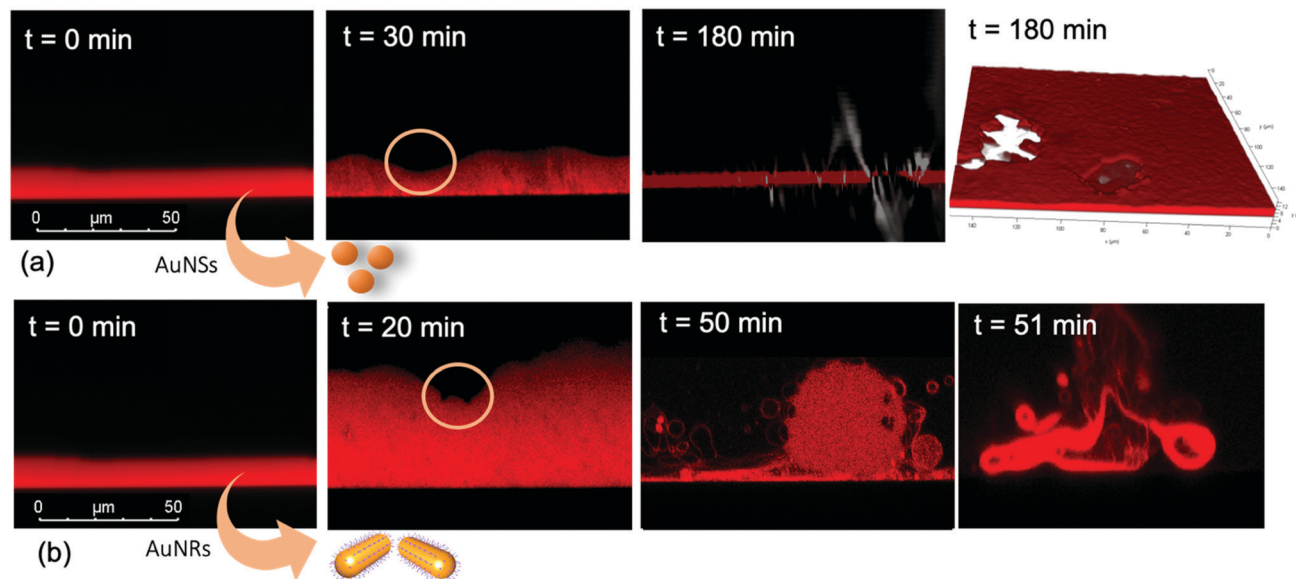
times from formation (from 0 to 10 s) have been acquired in fluorescence and transmission mode. This allowed us to simultaneously capture the fluorescence of the Nile Red labelled lipid matrix, and the gold nanoparticles. Representative images acquired within 10 s from the droplet formation are reported in Fig. 8a. At the beginning of the process, AuNRs, which can be visualized as black spots in the image, are located as micron-sized clusters at the edges of the spherical lipid droplet. Then, they start to excavate and unroll the lipid droplet starting from the edges of the sphere. This led to the complete collapse of the sphere within 10 s (see also the ESI,† video). In addition, it is possible to further analyse the mechanism of interaction of AuNRs with the lipid films by monitoring their excavation of the film in detail (Fig. 8b). Briefly, the AuNRs concentrate at the edges of the film as clusters, which progressively interact with the lipid interface and erode it. Interestingly, these clusters (which are highlighted with a zoom in Fig. 8b), appear to be elongated, which suggests that they are formed by end-to-end interactions of the AuNRs. On the contrary, for AuNSs only small clusters of round shape appear on the lipid film (see ESI,† Fig. S3). It is worth pointing out that, while cationic AuNSs and AuNRs form a stable dispersion in water, their lipid membrane-induced clustering is a clear hallmark of the strong interaction occurring at the nano-bio interface, as shown in several studies, both on synthetic and on biogenic lipid membrane.[29,41,42] This is likely due to the attractive interaction of the nanoparticles with the lipid membrane driven by *e.g.* electrostatic, hydrophobic and van der Waals interactions. This leads to the accumulation of the particles at the interface that promotes aggregation. In addition, for the cationic nanoparticles, the interaction with a membrane with an apparent

negative net-charge leads to a reduction of nanoparticle charge that further promotes aggregation. Overall, the results gathered lead to two main conclusions: (i) in agreement with the Neutron Reflectivity analysis, the impact of AuNRs on both lamellar and cubic model films is stronger and leads to faster structural and morphological modifications with respect to AuNSs; (ii) NPs interact with lamellar and cubic phases according to two different and well-defined mechanisms, *i.e.* the peeling-off of the lamellar assembly and the excavation-dewetting of the cubic phase assembly.

The role of symmetry in NPs-lipid films interactions

The experimental results obtained with the different combined experimental techniques give a clear picture of the role that structure and morphology play to control NPs interactions with model membrane at different length scales. The mechanism is strongly affected by the structure of both the lipid film, *e.g.* the phase behaviour, and morphology, *i.e.* shape asymmetry of the NPs, as briefly summarized in Fig. 9.

The effect of NPs shape asymmetry. Both Neutron Reflectivity and CLSM results point out a major role of NPs asymmetric shape in the interaction with model membranes. Neutron Reflectivity results show that AuNRs have a profound impact on the structure of both lamellar and cubic films, where a complete loss of structural order occurs in less than 15 min and after 2 h for Lα and *Pn3m* phases, respectively. On the contrary, the combination of Neutron Reflectivity and GISANS analyses shows a significantly less effect of the AuNSs on the lipid films. Indeed, we only detected a partial disruption of lamellar and cubic structures after 13 h and 32 h of incubation, respectively. The slightly higher zeta potential of AuNRs as
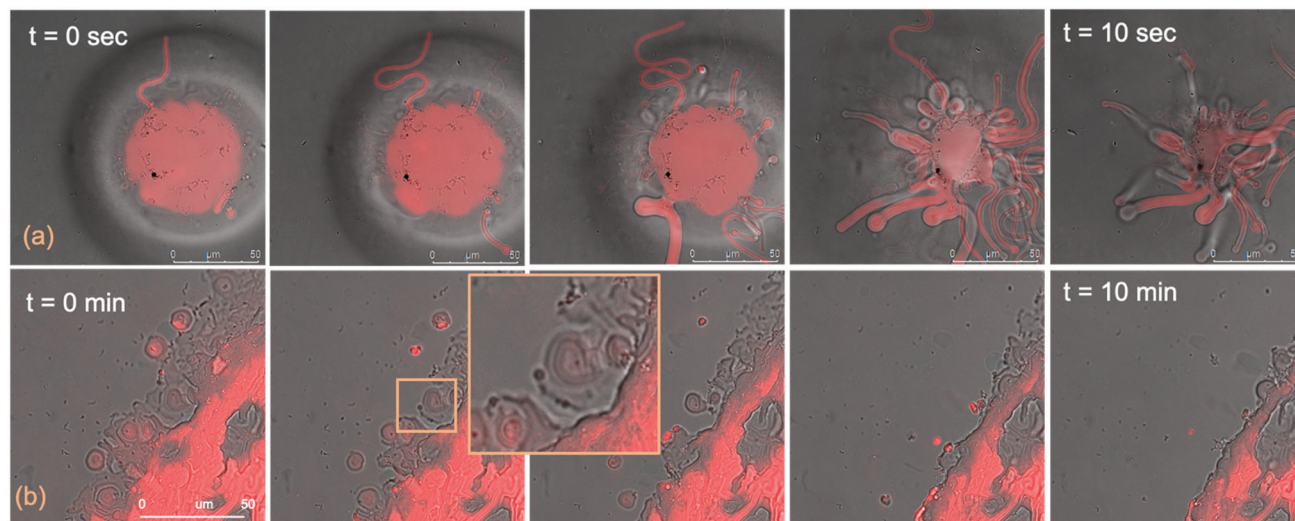
Fig. 8 CLSM images of AuNRs interacting with a GMO cubic film (overlay of fluorescence and transmission images): (a) disruption mechanism of a cubic film dewetted droplet by AuNRs, through the sequential extraction of lipid tubules from the bulk. (b) Mechanism of film excavation by AuNRs. Here, *t* = 0 corresponds to a lipid films/AuNRs incubation time ∼0 s, as the time needed for each image recording is less than 1 s.

compared to AuNSs could be considered as relevant in driving their stronger interaction with lipid interfaces; however, CLSM findings clarify that NPs shape is the main factor at play: when challenging lipid films, AuNRs form elongated clusters, which seem to be particularly effective in eroding the lipid films (Fig. 8b). In addition, tubules extraction phenomena are highlighted for AuNRs disrupting dewetted lipid films droplets (Fig. 8a), which are a typical feature of AuNRs interacting with other lipid interfaces.[29]

Our results are consistent with other studies, according to which the impact of NPs surface functionalization, composition and size on lipid membranes are recognized as the key determinants in NPs cytotoxicity.[1,5,29,42–46] However, much less is known on the effect of the NP shape on both model and natural biomembranes, and some of the reported observations are contradictory. Asymmetric NPs have a higher surface area/volume ratio, which is theoretically predicted to maximize the surface available to interact and attach to membranes. The main driving forces here are van der Waals and possible electrostatic attractive forces,[1,16] as well as hydrophobic interactions, depending on the NPs properties. This has often been connected to a high affinity to bilayered biomimetic systems[29] and natural membranes,[47] which in turn has been linked to an enhanced cellular uptake.[48,49] On the other hand, the higher surface curvature at the edges of non-spherical NPs is predicted to increase the energy barrier required for the wrapping of the NPs by membranes, that can drive the internalization by cells.[3] Recent experimental findings report lower cellular uptake of asymmetric NPs compared to spherical ones.[14,15] In addition, to the best of our knowledge, the impact of NPs shape on their interaction with nonlamellar lipid films, mimicking curved bilayers, has not been studied before.

Here, employing spherical and rod-like AuNPs of comparable diameter and surface charge, we can separately study the effect of NPs shape on their interaction with membranes. We found that, when NPs size is similar to the lipid bilayer

thickness, shape is of major importance, with asymmetric geometries producing more destructive effects on the lipid film structure and integrity. In particular, CLSM results suggest that, thanks to their asymmetric nature, AuNRs are able to maximize their interfacial interaction with lipid films, by forming end-to-end elongated clusters, while AuNSs seem to form more spherical clusters. Our results suggest that formation of the NPs elongated clusters facilitate the extraction of lipid tubules from the film. Eventually this was found leading to the complete erosion and disruption of the layer (see Fig. 9 scheme). Importantly, this behaviour was observed for both lamellar and non-lamellar films, highlighting a universal effect of NPs asymmetry on membranes of different structures.

The effect of membrane phase structure. Besides NPs shape, we found that membrane phase structure is another key factor that controls NPs interactions. Neutron Reflectivity and CLSM analyses highlighted that, for a given NP type, membrane geometry determines both the strength, pathway and results of interaction with NPs. Specifically, our Neutron Reflectivity results show that, independently from their shape, NPs induce a faster disruption of the nanostructure of lamellar films compared to cubic ones. This results into faster morphological modifications at the micron-scale as observed using CSLM. By combining the Neutron Reflectivity and CSLM data, we defined two different mechanisms that describe the interaction of NPs with lamellar and cubic phases and are responsible for their different stability towards nanomaterials (see Fig. 9).

The faster structural modification of Lα films induced by both AuNSs and AuNRs (Neutron Reflectivity and GISANS analyses) is associated with an initial swelling, followed by a progressive exfoliation of the multilamellar arrangement (CSLM analysis), that proceeds from the outer lamellar layers. We can hypothesize that, after their injection, NPs start to penetrate the outer part of the lamellar arrangement, *i.e.* the part directly exposed to water. This penetration would primarily
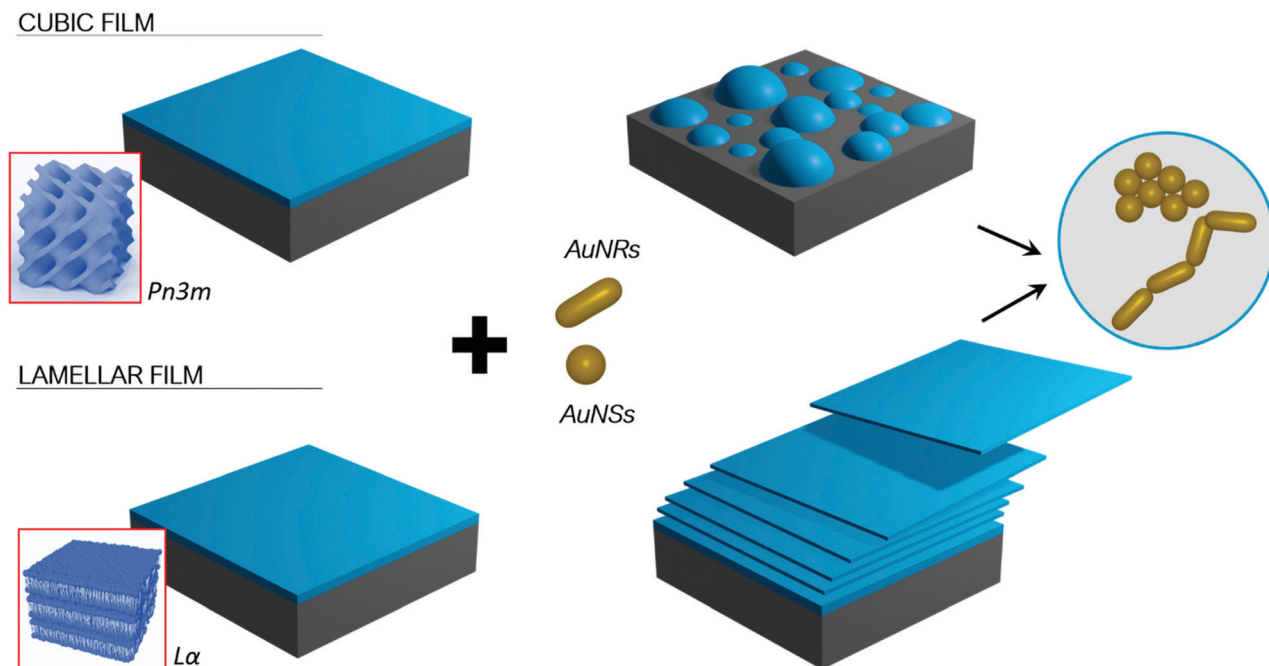
Fig. 9 Schematic illustration of the results of the interaction between AuNPs and cubic and lamellar phase lipid films. AuNPs induce the excavation and then dewetting of the cubic films (on the top), while provoking a progressive exfoliation of the lamellar arrangement (on the bottom). The disruption of both cubic and lamellar films is faster with AuNRs than with AuNSs, related to the different clustering processes of AuNPs interacting with lipid membranes, *i.e.* symmetrical clustering of AuNSs *versus* edge-to-tail asymmetric aggregation of AuNRs.

occur thanks to electrostatic and dipolar interactions between the cationic coating of NPs and the polar headgroup of lipids composing the membrane. This interaction would enable the insertion of NPs, together with their hydration shell, within the hydrophilic domains of the phase, *i.e.* the water layers separating the different lamellae. Then, the mismatch between the thickness of the water layers (around 2–3 nm) and NPs hydrodynamic size of about 4–5 nm (see Dynamic Light Scattering results in the ESI†) would be responsible for the initial swelling of the lamellar film. This is likely due to the insertion of NPs of larger size than the lamellar spacing and observed through CSLM. The increasing inter-lamellar distance would reduce the interactions between different lamellae, producing the detachment of the outer lamellar layers, which are the first ones to be in contact with NPs. Indeed, lipid bilayers of equal composition are held together only by weak van der Waals forces, in equilibrium with repulsive electrostatic and entropic contributions.[50] Thus, inter-bilayer interactions are easily overcome by attractive single bilayer-NPs forces mainly of electrostatic nature. The thinning of the film favors the penetration of NPs deeper into the film, *i.e.* coming closer to the solid support and promoting progressive peeling-off the lipid film. The loss of the lamellar periodicity as the layers are being detached can be connected with the progressive smearing out of the Lα-structural features, observed through Neutron Reflectivity (Fig. 2, 4 and 5).

On the other hand, a different interaction mechanism can be expected for the case of cubic phase films, accounting for their higher structural stability. Neutron Reflectivity and GISANS data highlight a progressive disordering and disruption

of the cubic *Pn3m* nanostructure induced by NPs, which starts from the shrinkage of its lattice parameter (see GISANS analysis). This nanoscale phenomenon coincides with a progressive excavation of the film observed at the micron-scale (CSLM analysis), leading to de-wetting. Interestingly, this phenomenon proceeds from NPs clusters, which, acting like micron-sized "diggers", progressively erode and unroll the lipid matrix. We can hypothesize that, in this case, NPs are not able to fully penetrate the internal aqueous region of the film. Indeed, cubic phases represent a 3D highly interconnected network, where a continuous lipid bilayer folds in the space originating bicontinuous lipid and aqueous domains,[20] where the aqueous nanochannels has a diameter of around 4.4 nm. This liquid crystalline 3D architecture with intertwined systems of water channels of similar size as NPs would impede their full insertion; indeed, in the Lα phase, different lamellae can progressively detach the one from the other, with minimal energy required at each detachment step. On the contrary, the swelling of the cubic arrangement induced by the insertion of NPs would result in a modification of the whole cubic arrangement, due to its highly interconnected (*i.e.* bicontinuous) nature, which would involve an higher energy cost. Instead, the attractive NPs-lipid headgroups forces would result in the absorption of NPs, residing onto the film surface as clusters (see Fig. 8 and Fig. S3 of ESI†). As highlighted by Neutron Reflectivity analysis, their presence induces an immediate shrinking of the phase, leading to local release of water and dehydration of the phase. We can speculate that this phenomenon drives the progressive collapse of the cubic arrangement. Such process would then

proceed from the different points where NPs accumulate across the membrane. Ultimately this leads to isolated lipid droplets onto the solid substrate.

The enhanced stability of cubic phases compared to lamellar ones might have important biological implications. As already discussed, curved membranes assembled with cubic symmetry are known to form in cells under certain conditions (*e.g.*, viral infection, oxidative stress, starving, membrane fusion and formation of extracellular vesicles). However, cubic membrane-related investigations have been limited to a descriptive level, while the biological function of these arrangements remains unexplored.[20]

Engineered NPs often have a similar size range as biologically relevant entities (*i.e.*, DNA, surface proteins, biogenic extracellular vesicles, and viruses), often resulting in similar interaction pathways with cells.[1] Thus, we might connect the higher resilience exhibited by cubic membranes towards NPs with a similar behaviour towards natural nano-objects, such as viral pathogens. Within this perspective, our results seem to suggest a possible "protective role" of the cubic architecture, occurring in critical cell conditions to minimize the membrane response towards harmful external perturbations.

To summarize, we found that NPs-lipid membrane interactions depend both on the nanostructure of the membrane and the shape of NPs. These two variables represent two sides of the same coin, as a single parameter, *i.e.* symmetry, can describe their variations. In these terms, we can state that NPs with asymmetric shape promote a stronger interaction with the lipid matrix. On the other hand, when referring to the structure and morphology of the lipid membrane, we observed that flat 2D membranes experience more substantial disruptive effects than curved ones with 3D symmetry when exposed to NPs. Importantly, we also pointed out that a variation in NPs symmetry only affects the strength of interaction with lipid films, but not the interaction pathway; on the contrary, membranes with different morphologies lead to completely different interaction mechanisms. This is the basis for the observed differences in the structural resilience of these systems.

Experimental

Materials

Tetrachloroauric(III) acid ($\geq$99.9%), (11-mercaptoundecyl)-*N*,*N*,*N*-trimethylammonium bromide ($\geq$90%), cetyl trimethyl ammonium bromide (99%), octanethiol (98.5%), ascorbic acid (98%), AgNO$_3$ (99%), HCl, toluene (99.8%), MeOH (99.8%), EtOH (99.8%), CHCl$_3$ (99%), tetraoctylammonium bromide (98%), NaBH$_4$ (98%), *n*-hexane (99%), 1,2-dioleoyl-*sn*-glycero-3-phosphocholine (DOPC) and Nile Red ($\geq$98%) were provided by Sigma-Aldrich (St. Louis, MO). A glycerol monooleate sample (mono- and diglycerides ratio 44:1 by weight), denoted as RYLO™ MG19 Glycerol Monooleate (GMO), was produced and provided by Danisco Ingredients (now Dupont, Brabrand, Denmark) with the following fatty acid composition (Lot No. 2119/65-1): 89.3% oleic, 4.6% linoleic, 3.4% stearic and 2.7%

palmitic acid. All chemicals were used as received. Milli-Q grade water was used in all preparations.

Synthesis of gold nanospheres (AuNSs)

Gold nanospheres functionalized with the cationic derivative *N*,*N*,*N*-trimethyl(11-mercaptoundecyl)ammonium bromide (TMA) were synthesized as described by McIntosh *et al.*[27,28] First, octanethiol-capped spherical gold nanoparticles (NSs) were prepared following the two-phase method developed by Brust *et al.*:[25,26] an aqueous solution of HAuCl$_4$ (15 mL, 30 mM) was mixed with a solution of tetraoctylammonium bromide (TOAB) in toluene (40 mL, 50 mM). The two-phase mixture was vigorously stirred until all the HAuCl$_4$ was transferred from the aqueous solution into the organic phase; TOAB acts as the phase-transfer reagent. Octanethiol (7.81 μL) was then added to the organic phase. A freshly prepared aqueous solution of sodium borohydride (12.5 mL, 0.4 M) was slowly added with vigorous stirring. On addition of the reducing agent, the organic phase changed colour from orange to deep brown within a few seconds. After further stirring for 3 h, the organic phase was separated, evaporated to 5 mL in a rotary evaporator and mixed with 200 mL ethanol to remove excess thiol. The mixture was kept for 4 h at −18 °C until a dark brown precipitate was formed, and the supernatant was removed with a pipette; the precipitate was washed with 200 mL of ethanol and put again in the freezer. After 4 h, the ethanol supernatant was removed with a pipette and completely evaporated in a rotary evaporator, obtaining octanethiol-capped gold nanoparticles. NSs capped with TMA were prepared by stirring 100 mg of octanethiol-capped NSs and 150 mg of *N*,*N*,*N*-trimethyl(11-mercaptoundecyl)ammonium bromide in 20 mL of degassed tetrahydrofuran under argon for two days at room temperature. The black precipitate of the gold nanoparticles was purified by repeated suspension, centrifugation, and decantation with dichloromethane. NSs capped with TMA were then dissolved in pure water without the need for pH adjustment. Such NPs have been found to be face-centered cubic (fcc) polyhedral.[51,52]

Synthesis of gold nanorods (AuNRs)

Gold NRs were synthesized according to a newly developed seedless growth protocol by El-Seyed.[53] Briefly, HAuCl$_4$ (5.0 mL; 1.0 mM) was added to 5.0 mL of Cetyl trimethyl ammonium bromide (CTAB, 0.2 M) at 27 °C, under magnetic stirring. Then, AgNO$_3$ (250 μL; 4.0 mM) was added. Subsequently, HCl (8.0 μL, 37%) was added to obtain a pH of 1–1.15. Then, we added 70 μL ascorbic acid (78.8 mM) under magnetic stirring and waited until the solution was clear. Immediately afterward, Ice-cold NaBH$_4$ (15 μL; 0.01 M) was added and allowed to react overnight. The final dispersion of AuNRs capped with CTAB was characterized by a dark pink colour. The excess of CITAB was removed from the dispersion by 10 cycles of centrifugation, each followed by precipitation of CITAB crystals and removal of the supernatant containing AuNRs. This AuNRs have been found to be single crystals of face-centered cubic (fcc) structure, with one of the main cubic axes oriented along the length of the rod.[54]

Preparation of lamellar and cubic lipid films

We obtained lamellar and cubic phase lipid films from GMO/DOPC 50/50% mol/mol and pure GMO, respectively. The lipid solutions in n-hexane (30/70 lipid/hexane % w/w) were spin-coated onto a solid substrate for 10 s at 700 r.p.m and then for 60 s at 2000 r.p.m. Most of the solvent evaporates during this procedure. The lipid-coated substrate was then immediately immersed in excess Milli Q water, leading to lamellar or cubic lipid films by hydration. For the case of lipid films prepared for CLSM analysis, lipid formulations were labelled with the hydrophobic dye Nile Red (0.1 mol% with respect to the total lipid amount), enabling the visualization of lipid layers; 100 μL of the lipid solution in n-hexane were deposited onto a hydrophilic round glass substrate (diameter of 15 mm) prior to spin-coating. Lipid films formed onto the glass substrate were then sealed into a single-well sample holder and hydrated with 2 mL of water before imaging. For the case of Neutron Reflectivity analysis, samples were formed by depositing 1 mL of n-hexane lipid solution on $50 \times 80 \times 15$ mm^3 ultra-polished Silicon n-doped single crystal (100) oriented (Siltronix, Archamps-France for the experiments performed at ISIS and Andrea Holm GmbH, Tann, Germany; roughness ≤ 5 Å for the experiments performed at MLZ) to cover almost the whole surface. After spin-coating and hydration, the substrate was sealed into a flow-cell type sample holder. To remove any excess contamination and the remaining n-hexane, an excess of water (at least 25 times the sample cell volume, *i.e.* 1.8 mL) was flushed through the sample cell. Silicon substrates were preliminary rinsed in either ultrapure water and ethanol, in order to remove organic residues. After that, they were bath sonicated for 30 min in ethanol with a Bandelin DL 102 3 L bath sonicator, followed by other 30 min in ultrapure water (Millipore Simplicity UV). The surfaces were then cleaned with a Novascan PSD-UV8 UV/ozone plasma for 30 min and rinsed in ultrapure water. Finally, they were dried with nitrogen gas and stored in ultrapure water, ready for deposition.

Neutron reflectivity

Static Neutron Reflectivity measurements (Section Synthesis of gold nanospheres (AuNSs)) were carried out at the OFFSPEC reflectometer[55] (Isis Neutron and Muon Source, Rutherford Appleton Laboratory, UK).

Neutrons in the wavelength range 1.0–14.5 Å were used to perform the measurements. Two incident angles, 0.50 deg and 2.00 deg allowed collecting data in the range $0.008 \leq Q/\text{Å}^{-1} \leq 0.3$. The arrival times and positions of scattered neutrons were detected on a ^{3}He 1×300 mm linear scintillator area detector (1.2 mm pixel size) positioned at 3.5 m from the sample. The linear detector also recorded the off-specular reflectivity in the vertical direction, which yields information about the in-plane structure at the interface. The detector consists of 768 wavelength shifting fibres with 0.5 mm pitch, resulting in an observable Q_x range of -6.5×10^{-4} to 6.5×10^{-4} Å^{-1}. The observable Q-range corresponds to real space distances, d, of approximately 1–40 mm (real and reciprocal space are related *via* $d = 2\pi/Q$). The set-up allows for a $\Delta Q_z/Q_z$ resolution of 2–5%.

In order to achieve a good signal-to-noise ratio, a counting time of about 5 h for the measurement was used.

Neutron Reflectivity kinetic measurements were performed at the REFSANS Horizontal TOF reflectometer operated by the Helmholtz-Zentrum Hereon at the Heinz Maier-Leibnitz Zentrum (MLZ) in Garching, Germany.[56] Neutrons in the wavelength range 3.0–21.0 Å were used to perform the measurements. A vertically collimated beam having a width of 40 mm was used to maximise the intensity. An incident angle of 3.0 deg allowed collecting data in the range $0.032 \leq Q/\text{Å}^{-1} \leq 0.22$ with a resolution of $\Delta Q_z/Q_z = 8\%$. In this way we cover the region in which the evolution of Bragg peaks as well as that of the off-specular scattering may be followed as a function of time. The arrival times and positions of scattered neutrons were detected on a Denex 2D 500×700 mm^2 multiwire ^{3}He detector (pixel size 2.1×2.9 mm^2, efficiency 80% at 7 Å, gamma sensitivity $<10^{-6}$) positioned at 4.5 m from the sample. The detector was installed in a liftable vacuum tube forming an angle of 5.2 deg with respect to the horizon. Reflectivities were acquired at time intervals of 5 min, over a time of 5 h. Raw data were reduced and converted to Q-space images, obtaining Q_x/Q_z maps.[57]

In all the evaluations, the vertical component Q_z was corrected for the ballistic effect due to the gravitational field.

Grazing incidence small angle neutron scattering (GISANS)

GISANS measurements were performed at the REFSANS, using most of the same settings adopted for carrying out Neutron Reflectivity measurements. The only differences concern the wavelength band composing the incident beam (ranging from 2.7 to 18.1 Å with a wavelength resolution $\Delta \lambda/\lambda = 5\%$), which corresponds to different penetration depths within the sample. A radial collimator was used to focus the beam on the detector, placed at 10.2 m from the sample. Acquired data were divided in wavelength slices having a width of 10% with respect to the mean value. For a given wavelength slice, the two-dimensional intensity data sets describe different (Q_y, Q_z) ranges. As for the Neutron Reflectivity investigations, z represents the direction which is normal to the liquid/nanoparticle interface; x indicates the beam direction oriented towards the scattering beam, whereas y is the remaining axis defining a levogyrous cartesian system. Also for the GISANS analysis, the Q_z component was corrected for the ballistic effect.

GISANS was employed to investigate films' properties along the directions perpendicular and parallel to the substrate interface. The in-plane film structure can be studied from the scattering patterns on the (Q_y, Q_z) plane. If α_i and α_f are the angles of incidence and reflection of the neutron beam, respectively, then the three spatial components of the scattering vector (which is defined as the difference between the wave vector of the scattered beam $\vec{k}_f$ and that of the incident beam $\vec{k}_i$ are:

$$\begin{bmatrix} Q_x \\ Q_y \\ Q_z \end{bmatrix} = \frac{2\pi}{\lambda} \begin{bmatrix} \cos\alpha_f \cos 2\theta_f - \cos\alpha_i \\ \cos\alpha_f \sin 2\theta_f \\ \sin\alpha_i + \sin\alpha_f \end{bmatrix}$$

This journal is © the Owner Societies 2022

Phys. Chem. Chem. Phys., 2022, **24**, 2762–2776 | **2773**

where λ is the neutron wavelength, while $2\theta_f$ indicates the scattering angle in the xy plane, which is relevant to determine lateral correlation lengths. The angle of incidence (0.5 deg) was chosen to get slices above and below the wavelength-dependent critical angle for total reflection (α_c).

Confocal laser scanning microscopy

A Leica CLSM TCS SP8 confocal microscope, operating in inverted mode, with a 63×1.3 numerical aperture water immersion objective, was used to image the lipid-based surface structures in excess water. The fluorescence of Nile Red lipophilic dye was excited at 561 nm and the fluorescence was acquired in the 571–650 nm emission range, with a PMT. Images were taken with a resolution of 512×512 pixels using a 400 Hz bidirectional scan with each scanning line averaged four times. Leica software was used to create three-dimensional reconstructions of the z-stacks.

Conclusions

In this contribution we explored the impact of symmetry and shape anisotropy on nano-bio interactions, focusing both on the geometry of nanoparticles and on the symmetry of the target membrane. By combining structural techniques with nanoscale resolution with Confocal Microscopy imaging, we connected structural and morphological modifications of lipid films induced by NPs, occurring at different length scales. Overall, our results show that breaking the 3D symmetry at the nano-bio interface (passing from a 3D sphere to a 1D rod in the NPs and from a 3D cubic phase to a 2D lamellar phase in the lipid film) results in an enhanced interaction. In addition, our findings provide new hints on the role of cubic membranes in Nature. Indeed, the biological function of cubic membranes occurring in stressed or starving cells,[58] or in cells exposed to infectious agents is, to date, debated: cubic membranes might result from aberrant membrane protein and/or lipid interactions in infected or pathological states, or might be a specific cellular response to these pathologies.[19] For instance, it has been hypothesized that viruses dysregulate cholesterol homeostasis of the host, to promote the formation of a cubic membrane as a protective environment to facilitate virus assembly and proliferation.[59] However, other studies hypothesize that the transformation from lamellar to cubic membranes is an adaptive strategy of cells under unhealthy conditions, as a method of defence.[60] Our results on cubic films, highlighting a striking higher resilience of cubic films as compared to lamellar ones towards NPs, support this latter hypothesis, suggesting a protective function of cubic membranes, which is inherently related to their 3D symmetry. Indeed, in this perspective, cubic membranes would represent biological barriers with enhanced structural resilience, occurring in cells as a "last defence" under extreme conditions, as in infected, stressed, or starved cells.

Conflicts of interest

There are no conflicts to declare.

Acknowledgements

References

1 M. Mendozza, L. Caselli, D. Berti and A. Salvatore, Nanoparticles and organized lipid assemblies: from interaction to design of hybrid soft devices inorganic stimuli responsive, *Soft Matter*, 2019, **15**, 8951–8970.

2 R. Michel and M. Gradzielski, Experimental Aspects of Colloidal Interactions in Mixed systems of liposome and inorganic nanoparticle and their applications, *Int. J. Mol. Sci.*, 2012, **13**, 11610–11642.

3 S. Dasgupta, T. Auth and G. Gompper, Nano- and microparticles at fluid and biological interfaces, *J. Phys.: Condens. Matter*, 2017, **29**, aa7933.

4 C. M. Beddoes, C. P. Case and W. H. Briscoe, Understanding nanoparticle cellular entry: a physicochemical perspective, *Adv. Colloid Interface Sci.*, 2015, **218**, 48–68.

5 A. M. Farnoud and S. Nazemidashtarjandi, Emerging investigator series: interactions of engineered nanomaterials with the cell plasma membrane; what have we learned from membrane models?, *Environ. Sci.: Nano*, 2019, **6**, 13–40.

6 M. Henriksen-Lacey, S. Carregal-Romero and L. M. Liz-Marzán, Current challenges toward *in vitro* cellular validation of inorganic nanoparticles, *Bioconjugate Chem.*, 2017, **28**, 212–221.

7 E. Blanco, H. Shen and M. Ferrari, Principles of nanoparticle design for overcoming biological barriers to drug delivery, *Nat. Biotechnol.*, 2015, **33**, 941–951.

8 P. Falagan-Lotsch, E. M. Grzincic and C. J. Murphy, One low-dose exposure of gold nanoparticles induces long-term changes in human cells, *Proc. Natl. Acad. Sci. U. S. A.*, 2016, **113**, 13318–13323.

9 C. J. Murphy, A. M. Vartanian, F. M. Geiger, R. J. Hamers, J. Pedersen, Q. Cui, C. L. Haynes, E. E. Carlson, R. Hernandez, R. D. Klaper, G. Orr and Z. Rosenzweig, Biological responses to engineered nanomaterials: needs for the next decade, *ACS Cent. Sci.*, 2015, **1**, 117–123.

10 L. Caselli, A. Ridolfi, J. Cardellini, L. Sharpnack, L. Paolini, M. Brucale, F. Valle, C. Montis, P. Bergese and D. Berti, A plasmon-based nanoruler to probe the mechanical properties of synthetic and biogenic nanosized lipid vesicles, *Nanoscale Horiz.*, 2021, **6**, 543–550.

11 K. L. Chen and G. D. Bothun, Nanoparticles Meet Cell Membranes: Probing Nonspecific Interactions using Model Membranes, *Environ. Sci. Technol.*, 2014, **48**, 873–880.

12 A. H. Bahrami, Orientational changes and impaired internalization of ellipsoidal nanoparticles by vesicle membranes, *Soft Matter*, 2013, **9**, 8642.

13 S. Dasgupta, T. Auth and G. Gompper, Wrapping of ellipsoidal nano-particles by fluid membranes, *Soft Matter*, 2013, **9**, 5473–5482.

14 S. Dasgupta, T. Auth and G. Gompper, Shape and orientation matter for the cellular uptake of nonspherical particles, *Nano Lett.*, 2014, **14**, 687–693.

15 R. Vácha, F. J. Martinez-Veracoechea and D. Frenkel, Receptor-mediated endocytosis of nanoparticles of various shapes, *Nano Lett.*, 2011, **11**, 5391–5395.

16 Q. Mu, G. Jiang, L. Chen, H. Zhou, D. Fourches, A. Tropsha and B. Yan, Chemical Basis of Interactions Between Engineered Nanoparticles and Biological Systems, *Chem. Rev.*, 2014, **114**, 7740–7781.

17 E. Gonzalez Solveyra and I. Szleifer, What is the role of curvature on the properties of nanomaterials for biomedical applications?, *Wiley Interdiscip. Rev.: Nanomed. Nanobiotechnol.*, 2016, **8**, 334–354.

18 S. Nangia and R. Sureshkumar, Effects of nanoparticle charge and shape anisotropy on translocation through cell membranes, *Langmuir*, 2012, **28**, 17666–17671.

19 Z. A. Almsherqi, S. D. Kohlwein and Y. Deng, Cubic membranes: a legend beyond the Flatland * of cell membrane organization, *J. Cell Biol.*, 2006, **173**, 839–844.

20 Z. A. Almsherqi, T. Landh and S. D. Kohlwein, *Cubic Membranes: The Missing Dimension of Cell Membrane Organization*, Elsevier Inc., 1st edn, 2009, vol. 274.

21 Y. Deng and M. Mieczkowski, Three-dimensional periodic cubic membrane structure in the mitochondria of amoebae Chaos carolinensis, *Protoplasma*, 1998, 16–25.

22 D. P. Chang, J. Barauskas, A. P. Dabkowska, M. Wadsäter, F. Tiberg and T. Nylander, Non-lamellar lipid liquid crystalline structures at interfaces, *Adv. Colloid Interface Sci.*, 2015, **222**, 135–147.

23 A. P. Dabkowska, M. Valldeperas, C. Hirst, C. Montis, G. K. Pálsson, M. Wang, S. Nöjd, L. Gentile, J. Barauskas, N. J. Steinke, G. E. Schroeder-Turk, S. George, M. W. A. Skoda and T. Nylander, Non-Lamellar lipid assembly at interfaces: controlling layer structure by responsive nanogel particles, *Interface Focus*, 2017, **7**, 20160150.

24 A. Ridolfi, B. Humphreys, L. Caselli, C. Montis, T. Nylander, D. Berti, M. Brucale and F. Valle, Exploring the structure and mechanics of thin supported inverse bicontinuous cubic phase lipid films, *bioRxiv*, 2021, DOI: 10.1101/2021.03.29.437497.

25 S. Tatur and A. Badia, Influence of hydrophobic alkylated gold nanoparticles on the phase behavior of monolayers of DPPC and clinical lung surfactant, *Langmuir*, 2012, **28**, 628–639.

26 M. Brust, M. Walker, D. Bethell, D. J. Schiffrin and R. Whyman, Synthesis of Thiol-derivatised Gold Nanoparticles in a Two-phase Liquid-Liquid System, *J. Chem. Soc., Chem. Commun.*, 1994, 801–802.

27 C. M. McIntosh, E. A. Esposito, A. K. Boal, J. M. Simard, C. T. Martin and V. M. Rotello, Inhibition of DNA transcription using cationic mixed monolayer protected gold clusters, *J. Am. Chem. Soc.*, 2001, **123**, 7626–7629.

28 S. Tatur, M. Maccarini, R. Barker, A. Nelson and G. Fragneto, Effect of functionalized gold nanoparticles on floating lipid bilayers, *Langmuir*, 2013, **29**, 6606–6614.

29 C. Montis, V. Generini, G. Boccalini, P. Bergese, D. Bani and D. Berti, Model lipid bilayers mimic non-specific interactions of gold nanoparticles with macrophage plasma membranes, *J. Colloid Interface Sci.*, 2018, **516**, 284–294.

30 D. E. Sands, *Introduction to Cristallography*, W.A. Benjamin, Inc., New York, NY, 1969.

31 V. Cherezov, J. Clogston, Y. Misquitta, W. Abdel-Gawad and M. Caffrey, Membrane protein crystallization in meso: lipid type-tailoring of the cubic phase, *Biophys. J.*, 2002, **83**, 3393–3407.

32 G. Popescu, J. Barauskas, T. Nylander and F. Tiberg, Liquid crystalline phases and their dispersions in aqueous mixtures of glycerol monooleate and glyceryl monooleyl ether, *Langmuir*, 2007, **23**, 496–503.

33 N. Kučerka, S. Tristram-Nagle and J. F. Nagle, Structure of fully hydrated fluid phase lipid bilayers with monounsaturated chains, *J. Membr. Biol.*, 2006, **208**, 193–202.

34 R. Negrini and R. Mezzenga, Diffusion, molecular separation, and drug delivery from lipid mesophases with tunable water channels, *Langmuir*, 2012, **28**, 16455–16462.

35 P. Müller-Buschbaum, Grazing incidence small-angle neutron scattering: challenges and possibilities, *Polym. J.*, 2013, **45**, 34–42.

36 S. J. Richardson, P. A. Staniec, G. E. Newby, N. J. Terrill, J. M. Elliott, A. M. Squires and W. T. Góźdź, Predicting the orientation of lipid cubic phase films, *Langmuir*, 2014, **30**, 13510–13515.

37 R. Kampmann, M. Haese-Seiller, V. Kudryashov, B. Nickel, C. Daniel, W. Fenzl, A. Schreyer, E. Sackmann and J. Rädler, Horizontal ToF-neutron reflectometer REFSANS at FRM-II Munich/Germany: first tests and status, *Phys. B: Condens. Matter*, 2006, **385–386**, 1161–1163.

38 K. Yang and Y. Q. Ma, Computer simulation of the translocation of nanoparticles with different shapes across a lipid bilayer, *Nat. Nanotechnol.*, 2010, **5**, 579–583.

39 W. K. Fong, T. L. Hanley, B. Thierry, N. Kirby, L. J. Waddington and B. J. Boyd, Controlling the nanostructure of gold nanorod-lyotropic liquid-crystalline hybrid materials using near-infrared laser irradiation, *Langmuir*, 2012, **28**, 14450–14460.

40 P. Vandoolaeghe, A. R. Rennie, R. A. Campbell, R. K. Thomas, F. Höök, G. Fragneto, F. Tiberg and T. Nylander, Adsorption of cubic liquid crystalline nanoparticles on model membranes, *Soft Matter*, 2008, **4**, 2267–2277.

41 C. Montis, A. Salvatore, F. Valle, L. Paolini, F. Carlà, P. Bergese and D. Berti, Biogenic supported lipid bilayers as a tool to investigate nano-bio interfaces, *J. Colloid Interface Sci.*, 2020, **570**, 340–349.

42 T. Pfeiffer, A. De Nicola, C. Montis, F. Carlà, N. F. A. Van Der Vegt, D. Berti and G. Milano, Nanoparticles at Biomimetic

This journal is © the Owner Societies 2022

Phys. Chem. Chem. Phys., 2022, **24**, 2762–2776 | **2775**

Interfaces: Combined Experimental and Simulation Study on Charged Gold Nanoparticles/Lipid Bilayer Interfaces, *J. Phys. Chem. Lett.*, 2019, **10**, 129–137.

43 P. Vedantam, G. Huang and T. R. J. Tzeng, Engineered nanoparticles interacting with cells: size matters, *J. Nanobiotechnology*, 2013, **4**, 13–20.

44 C. Montis, L. Caselli, F. Valle, A. Zendrini, F. Carlà, R. Schweins, M. Maccarini, P. Bergese and D. Berti, Shedding light on membrane-templated clustering of gold nanoparticles, *J. Colloid Interface Sci.*, 2020, **573**, 204–214.

45 B. Pelaz, G. Charron, C. Pfeiffer, Y. Zhao, J. M. De La Fuente, X. J. Liang, W. J. Parak and P. Del Pino, Interfacing engineered nanoparticles with biological systems: anticipating adverse nano-bio interactions, *Small*, 2013, **9**, 1573–1584.

46 A. Ridolfi, L. Caselli, C. Montis, G. Mangiapia, D. Berti, M. Brucale and F. Valle, Gold nanoparticles interacting with synthetic lipid rafts: an AFM investigation, *J. Microsc.*, 2020, **280**, 194–203.

47 S. Salatin, S. Maleki and A. Y. Khosroushahi, Effect of the surface modification, size, and shape on cellular uptake of nanoparticles, *Cell Biol. Int.*, 2015, **39**, 881–890.

48 S. E. A. Gratton, P. A. Ropp, P. D. Pohlhaus, J. C. Luft, V. J. Madden, M. E. Napier and J. M. Desimone, The effect of particle design on cellular internalization pathways, *Proc. Natl. Acad. Sci. U. S. A.*, 2008, **105**, 11613–11618.

49 R. Agarwal, V. Singh, P. Jurney, L. Shi, S. V. Sreenivasan and K. Roy, Mammalian cells preferentially internalize hydrogel nanodiscs over nanorods and use shape-specific uptake mechanisms, *Proc. Natl. Acad. Sci. U. S. A.*, 2013, **110**, 1–6.

50 J. N. Israelachvili, *Intermolecular and Surface Forces*, 3rd edn, Elsevier, 2011.

51 T. Mori and T. Hegmann, Determining the composition of gold nanoparticles: a compilation of shapes, sizes, and calculations using geometric considerations, *J. Nanoparticle Res.*, 2016, **18**, 1–36.

52 S. I. Stoeva, B. L. V. Prasad, S. Uma, K. J. Stoimenov, P. K. Zaikovski, V. Sorensen and C. M. Klabunde, Face-Centered Cubic and Hexagonal Closed-Packed Nanocrystal Superlattices of Gold Nanoparticles Prepared by Different Methods, *J. Phys. Chem. B*, 2003, **107**, 7441–7448.

53 M. R. K. Ali, B. Snyder and M. A. El-Sayed, Synthesis and optical properties of small Au nanorods using a seedless growth technique, *Langmuir*, 2012, **28**, 9807–9815.

54 T.-S. Deng, J. E. S. van der Hoeven, A. O. Yalcin, H. W. Zandbergen, M. A. van Huis and A. van Blaaderen, Oxidative Etching and Metal Overgrowth of Gold Nanorods within Mesoporous Silica Shells, *Chem. Mater.*, 2015, **27**, 7196–7203.

55 R. M. Dalgliesh, S. Langridge, J. Plomp, V. O. De Haan and A. A. Van Well, Offspec, the ISIS spin-echo reflectometer, *Phys. B: Condens. Matter*, 2011, **406**, 2346–2349.

56 J.-F. Moulin and M. Haese, *REFSANS: reflectometer and evanescent wave small angle neutron spectrometer. Journal of large-scale research facilities*, J. large-scale Res. Facil. JLSRF.

57 A. Hafner, P. Gutfreund, B. P. Toperverg, A. O. F. Jones, J. P. de Silva, A. Wildes, H. E. Fischer, M. Geoghegan and M. Sferrazza, Combined specular and off-specular reflectometry: elucidating the complex structure of soft buried interfaces, *J. Appl. Crystallogr.*, 2021, **54**, 924–948.

58 R. Mezzenga, J. M. Seddon, C. J. Drummond, B. J. Boyd, G. E. Schröder-Turk and L. Sagalowicz, Nature-Inspired Design and Application of Lipidic Lyotropic Liquid Crystals, *Adv. Mater.*, 2019, **31**, 1–19.

59 Y. Deng, Z. A. Almsherqi, M. M. L. Ng and S. D. Kohlwein, Do viruses subvert cholesterol homeostasis to induce host cubic membranes?, *Trends Cell Biol.*, 2010, **20**, 371–379.

60 Q. Xiao and E. Al, Why Do Membranes of Some Unhealthy Cells Adopt a Cubic, *ACS Cent. Sci.*, 2016, **2**, 943–953.